Advances in the Development of the anodic Side of a CO_2 Electrolyzer: a more efficient Oxygen Evolution Catalyst and Alternative Oxidation Reactions

Internship Report

Robin Vogel

Daily Supervisors:
Michiel de Heer & Dr. Paul Corbett

First Examiner:
Prof. Petra E. de Jongh

August 31, 2020

Shell Technology Centre Amsterdam
The Netherlands

Abstract

The cost efficiency of a CO_2 electrolyzer can be improved by enhancing the performance of its anodic side. Therefore, we prepared the Sr_2GaCoO_5 oxygen evolution catalyst to see if this catalyst, composed of abundant materials, can compete with the benchmark IrO_2. X-ray diffraction analysis revealed that the desired phase was generated. The activity of Sr_2GaCoO_5 in comparison with IrO_2 was evaluated with linear sweep voltammetry. Sr_2GaCoO_5 facilitated oxygen evolution with an overpotential of 382 mV at 20 $\mu A \cdot cm^{-2}$, 102 mV higher than reported. The IrO_2 catalyst exhibited an overpotential of 288 mV at the same current density. In addition, the Sr_2GaCoO_5 was found to degrade within one hour of chronopotentiometry, whereas IrO_2 appeared to be highly stable. A second strategy for electrolyzer enhancement was explored with a literature review on partial electrochemical methanol oxidation towards mono ethylene glycol, formaldehyde and dimethyl carbonate.

Contents

Introduction

Climate change associated with CO_2 emissions led to an urgent need to shift from a fossil fuel to a sustainable energy industry.[1] Therefore, company's, such as Shell, are obliged change their business model in a radical manner. In this view, Shell commits to the development of a CO_2 electrolyzer, a system in which electrical power is used to drive the reduction of CO_2 into value added chemicals. This internship focuses on the improvement of the anodic part of the electrolyzer.
Electrochemical carbon dioxide reduction (ECO2RR) provides a strategy to store electrical energy in chemical bonds of various compounds such as carbon monoxide, formic acid, methane, ethylene and alcohols. By doing so, ECO2RR can provide a valid solution to major challenges in the field of renewable energies. The surplus of electrical power that arises as a result of the intermittent wind and solar power can be stored in versatile chemicals. The obtained chemicals can be used in a flexible manner within the existing infrastructure of the energy industry, as dense energy carriers for hard to abate sectors, or for the production of carbon based chemicals. A CO_2 to CO electrolyzer, shown in Figure 1.1a, can be implemented within Shell's existing infrastructure, linked to liquid to gas facilities. Here, hydrogen and CO are converted into liquid fuels.[2, 3, 4]
The electrons consumed for the reduction of CO_2 at the cathode of the electrolyzer are generated at the anode, typically with the oxygen evolution reaction (OER). OER is a kinetically sluggish reaction as it proceeds via four proton coupled electron transfers from two water molecules to yield O_2. Therefore, a high potential is needed to overcome the energy barrier of this reaction. As a result, OER lays a heavy burden on the energy efficiency of the integrated ECO2RR system. Approximately 90% of the power input is consumed by OER coupled with CO_2 to CO reduction. Therefore, we identified two strategies to enhance the performance of the electrolyzer; the employment of a more active OER catalyst and the execution of a kinetically more favourable alternative oxidation reaction that yields a value added product, illustrated with Figure 1.1b.[5, 6]
Recently, Zhou et al. reported Sr_2GaCoO_5 as a highly stable OER catalyst that facilitated OER at lower potential than the benchmark IrO_2 in neutral environment. An OER catalyst that performs well under neutral conditions is desirable. ECO2RR is commonly carried out in neutral solutions, running both the anodic and cathodic side of the electrolyzer at neutral pH greatly reduces the complexity and enhances the efficiency of an electrolyzer.[7] Here, we aim to prepare the Sr_2GaCoO_5 catalyst, reproduce the results obtained by Zhou et al. and apply the catalyst in our electrolyzer.
The second strategy for electrolyzer enhancement was explored with a literature review on alternative oxidation reactions that may be coupled with ECO2RR in an electrolyzer. The review covers partial electrochemical methanol oxidation towards mono ethylene glycol (MEG), formaldehyde and dimethyl carbonate (DMC). The synthesis of the latter product was deemed most promising. The review is placed in the outlook chapter as it may result in future experimental endeavors.

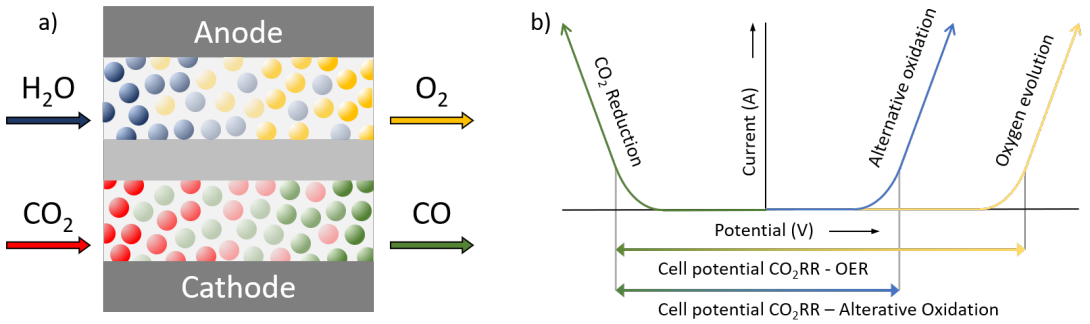

Figure 1.1: (a) The CO_2 electrolyzer. CO_2 is electrochemically converted into CO at the cathode. The OER occurs in the anodic compartment. (b) Strategies for enhancement of the efficiency of the anodic side of the electrolyzer. The cell potential can be lowered with the improvement of the OER catalyst or the execution of an alternative oxidation reaction.

Theoretical background

2.1 Electrochemistry

2.1.1 The current-potential relationship

The study of phenomena that occur on the anode and the cathode of an electrolyzer typically concerns the determination of the relationship between current and potential, illustrated with the solid curve in Figure 2.2b. An inspection of the curve reveals that no current flows trough the cell up to a certain potential. Once a current starts to flow, electrical energy is consumed to yield chemicals. The electrochemical active species are oxidised at the anode and reduced at the cathode. The reversible potential required to drive this uphill reaction can be determined with the Nernst equation.[8] This equation includes two terms; the driving force under standard conditions E^0 and a therm that takes the dependence on reagent concentrations and temperature into account. The Nernst equation for a Redox reaction is:

$$E_{rev} = E^0 - \frac{RT}{nF} ln \frac{[Red]^b}{[Ox]^a} \tag{2.1}$$

Where E^0 is reduction potential under standard conditions. R is the gas constant, 8.314 $J \cdot K^{-1} mol^{-1}$. T is the temperature (K), n is the number of electrons involved in the half-reaction. F is Faraday constant (9.649 10^4 $C \cdot mol^{-1}$) [Ox] and [Red] are the concentrations of the oxidising and reducing species involved in the reaction.

The E_{rev} is generally not the potential at which current starts to flow to yield product. The overpotential, η, is defined as the difference between the actual potential required to drive a reaction and the theoretically required reversible potential derived with the Nernst equation.

$$\eta = E - E_{rev} \tag{2.2}$$

The overpotential is mainly the result three physical phenomena, activation overpotential (η_{act}), concentration overpotential (η_{con}) and resistance overpotential (η_{res}). As a simplification, one can describe the overpotential as the sum of these three phenomena.

$$\eta = \eta_{act} + \eta_{con} + \eta_{res} \tag{2.3}$$

η_{act} is the kinetically significant quantity that is caused by the electrochemical energy required to overcome the activation barrier for the reaction. The transition of electrons from and towards species that are oxidised or reduced at the surface of an electrode is kinetically controlled. The surface of the electrode acts as an heterogeneous catalyst in essence. The interaction of the surface and the active species determines its catalytic properties. Figure 2.2a shows that a catalyst lowers the activation energy for a reaction. The lowered activation energy is electrochemically expressed in a lowered onset potential, illustrated with Figure 2.2b. The initial part of the rising curve in Figure 2.2b is activation controlled.
The current would rise exponentially if it were not for limitations caused by mass transport. Charge transfer and mass transport are two coupled processes. Therefore, the reaction rate and observed current is determined by the slower of the two. At low applied potential, the rate is limited by the transfer of charge to active species. Charge transfer ceases to influence the observed current at higher applied potentials. In this regime, mass transfer limits the reaction rate and the current is independent of the potential, illustrated by the flattening of the curve of Figure 2.2b. The concentration of reactants at the surface of the electrode lowers when they are consumed. It is necessary to apply an additional amount of potential in order to bring species from the bulk to the surface and maintain the same reaction rate. This process is responsible for the η_{con}.
The last considerable phenomenon that causes overpotential is the η_{res}, the result of the residual potential drop caused by the resistance of the electrolyte solution. This overpotential can be largely eliminated on laboratory scale. In addition, the resistance of the electrolyte solution can be measured and corrected for experimentally. It is however, from an economical point of view, good to keep in mind that this phenomenon causes enormous amounts of energy losses on industrial scale.[9]

From the perspective of this research, we are mainly interested in the catalytic properties of electrode materials. The activation controlled component of the onset potential, is a key descriptor of electrode kinetics. Therefore, we are obliged to insulate this form of overpotential from the other two. Experimental techniques described in the following section have been developed to facilitate this goal.

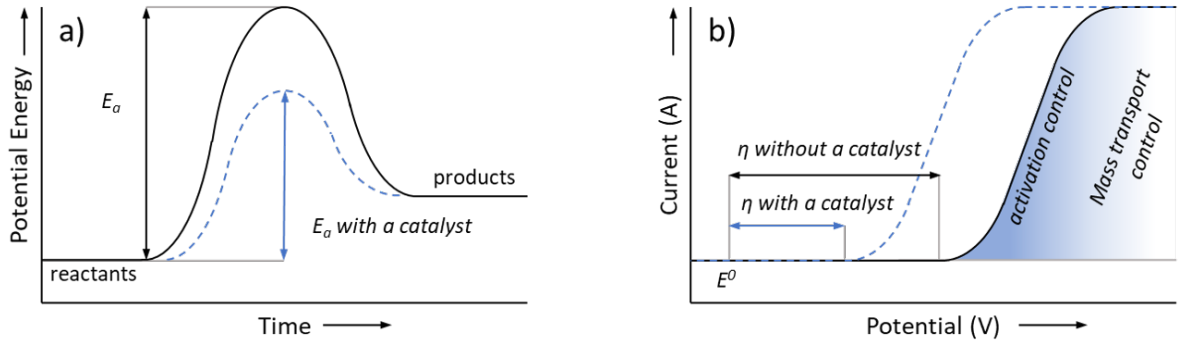

Figure 2.2: (a) Typical energy diagram of an electrochemical reaction, a catalyst lowers the activation energy. (b) Current-potential relationship. The lowered activation energy is electrochemically expressed in a lowered onset potential. The initial part of the rising curve is activation controlled. The rise of the curve is limited by mass transport effects.

2.1.2 Experimental techniques

Establishing the relation between current and potential that arises when an electrochemical reaction occurs provides insight in the catalytic properties of the employed electrode material.
A three-electrode setup, depicted in Figure 2.3, forms the basis upon which many electrochemical measurement techniques are based. This cell consists of two compartments; an anode at which the oxidation reaction occurs and a cathode at which the reduction reaction takes place. Both compartments are separated by a by a barrier that allows the passage of charged particles but prevents the crossover of reaction products. Usually, only one of the two electrodes is studied at a time. The reaction of interest occurs at the so called working electrode (WE), The reaction that closes the redox cycle occurs at the counter electrode (CE).
The relationship between current and potential at the WE is the key descriptor for electrocatalysis. In the three-electrode setup, a variable current source is employed to pass current through the CE and the WE. The passage of current causes a potential difference over the entire cell. This cell potential however, is the sum of several potential differences. The main differences are brought about by the voltage drop across the solution and the changes in potential across the interface of the cathode and the anode. The first component can be measured and corrected for. The potential of the WE is insulated from the potential of the CE with the aid of another circuit, with a reference electrode (RE). The RE has a highly stable reproducible potential that can be calculated with the Nernst equation. Practically no current passes trough the RE. Hence, its potential constant. Therefore, the change in potential between WE and RE equals the potential change of the WE.
Moving the electrode in solution provides an efficient strategy to improve mass transport. This can be accomplished in a highly reproducible manner with the aid of a rotating disc electrode (RDE), depicted in Figure 2.3b. The RDE is composed of a cylindrical metal rod embedded within a plastic cylindrical holder so that the bottom end of the metal is exposed to the solution. Rotation of the RDE effects the mass transport in a direction perpendicular to its surface. As a result of the rotation, the solution in the vicinity of the surface is pushed away sideways and replaced by solution pulled upwards from the bulk, in a direction perpendicular to the surface. Hereby, the surface effectively acts as a pump. By doing so, mass transport effects are limited.[9]

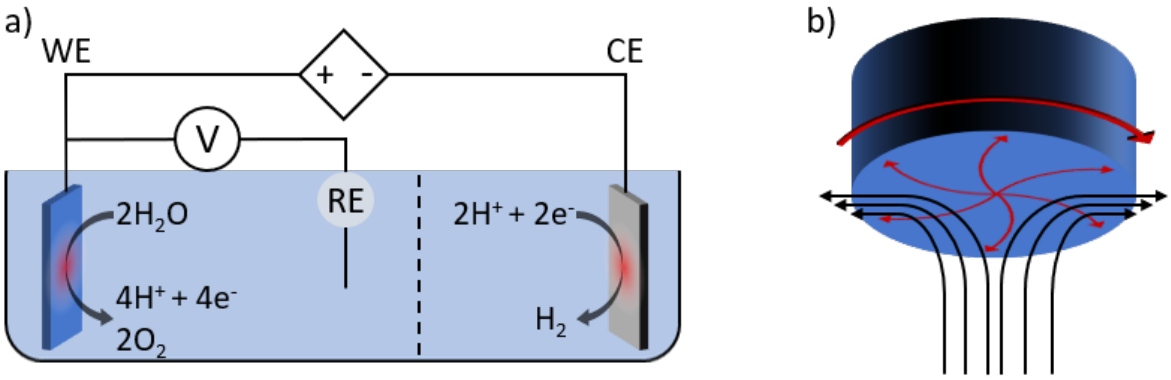

Figure 2.3: (a) Schematic overview of a typical three-electrode setup. The electrochemical reaction of interest, in this case, the OER, occurs at the WE. The redox cycle is closed with the hydrogen evolution reaction. The potential of the WE is determined with the RE. (b) Working principle of the rotating disk electrode

2.2 Oxygen evolution reaction

The oxygen evolution reaction (OER), where oxygen is generated via four proton coupled electron transfers, is pH dependent. In alkaline environment four hydroxyde ions are oxidized to yield two water molecules and oxygen. in acidic and neutral media, the reaction proceeds via the oxidation of two water molecules into four protons and an oxygen molecule. The equilibrium half-cell potential under standard conditions (E_a^0), 1 atm and 25 C, equals 0.404 V in alkaline solutions and 1.23 V in acidic or neutral solutions. Theoretical models suggest that the OER proceeds in four steps depending on the pH of the medium in which the reaction occurs. These steps are described in the following equations, The $*$ sign denotes surface adsorbed species.[10]

In alkaline Media:

$$OH^- \longrightarrow OH^* + e^- \tag{2.4}$$

$$OH^* + OH^- \longrightarrow O^* + H_2O + e^- \tag{2.5}$$

$$O^* + OH^- \longrightarrow OOH^* + e^- \tag{2.6}$$

$$OOH^* + OH^- \longrightarrow O_2 + H_2O + e^- \tag{2.7}$$

$$\textbf{Total: } \mathbf{4\,OH^-} \longrightarrow \mathbf{2\,H_2O + O_2 + 4\,e^-} \tag{2.8}$$

In acidic and neutral media:

$$H_2O \longrightarrow OH^* + H^+ + e^- \tag{2.9}$$

$$OH^* \longrightarrow O^*\,H^+ + e^- \tag{2.10}$$

$$O^* + H_2O \longrightarrow OOH^* + H^+ + e^- \tag{2.11}$$

$$OOH^* \longrightarrow O_2 + H^+ + e^- \tag{2.12}$$

$$\textbf{Total: } \mathbf{2\,H_2O} \longrightarrow \mathbf{4\,H^+\,O_2 + 4\,e^-} \tag{2.13}$$

All described steps are thermodynamically uphill when no potential is applied. The thermodynamically ideal catalyst equalises the barrier of all four charge transfer steps. In this case, all the reaction free energies are zero at the equilibrium potential of 1.23 V, illustrated with free energy diagram for the ideal OER catalyst in Figure 2.4a. In reality, catalysts do not behave ideally. The free energy diagrams of three catalysts $LaMnO_3$, $SrCoO_3$ and, $LaCuO_3$ that provide strong binding, intermediate binding and weak binding respectively are shown in 2.4 B, C and D. some, but not all of the steps become down hill

at 1.23 V. Hence, OER does not proceed. In addition the free energy diagram is plotted at a potential at which the rate determining step becomes downhill. From these plots it is evident that a suitable catalyst provides intermediate binding of the intermediates to facilitate the OER reaction at relative low potential. If the catalyst binds either to strong or to weak the, potential required to drive the reaction becomes higher.

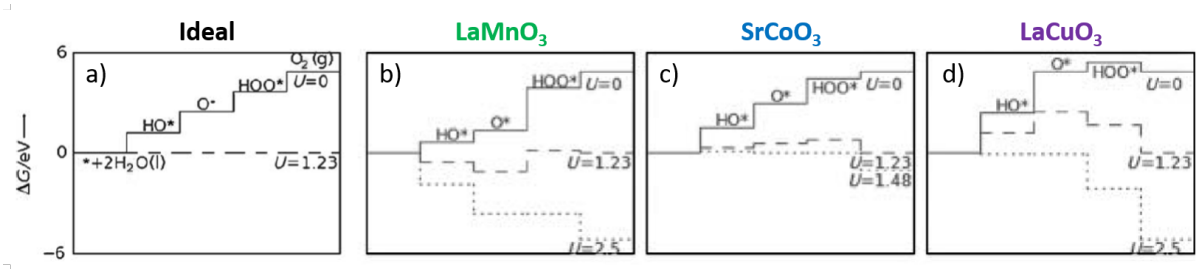

Figure 2.4: Free energy diagrams for OER of an ideal catalyst (a), $LaMnO_3$ (b), $SrCoO_3$ (c) and, $LaCuO_3$ (d) at 0 V, 1.23 V and the potential at which the last step becomes downhill. Adopted from ref [11]

It has been observed that the sum of the energies required for steps 2.5 and 2.6 and steps 2.10 and 2.11 is roughly constant. This phenomenon is illustrated in Figure 2.4. The difference between the energy levels of HO* and HOO* is roughly constant. This correlation is a so-called scaling relation. A low barrier for step 5 causes a higher barrier for step 6 and vice versa. The constant difference between the energy levels of HO* and HOO* gives that the catalytic activity can be described with the difference between ΔG O* and ΔG OH*. Plotting this value against the overpotential yields a volcano plot for a wide variety of metal oxide structures such as perovskites and rutiles, shown in Figure 2.5. A good catalyst binds the intermediates neither to strong, nor to weak and is therefore positioned on the top of the volcano plot with the highest activity an the lowest onset potential for OER.
Density functional theory calculation enable the calculation of the binding energies. OER has been studied using this method on metals, rutile oxides and perovskites. The scaling relation has been found to be universital for rutile, perovskite, spinal, rock salt and bixbytine oxides.[11]

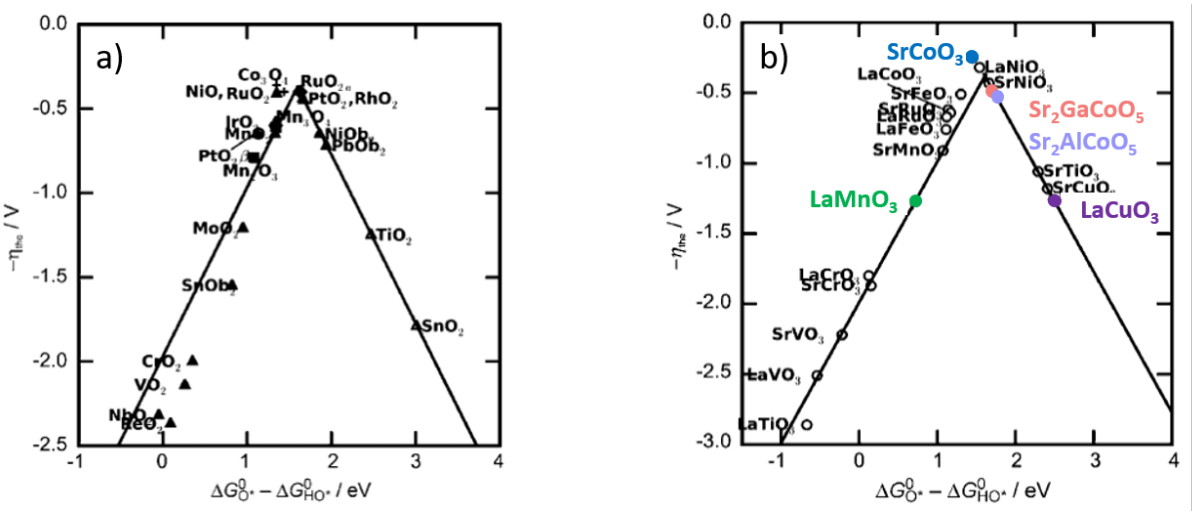

Figure 2.5: Volcano plot for OER activity for rutile (a) and perovskite (b) oxides adopted from ref. [11].

2.2.1 Catalysts for the oxygen evolution reaction

Choosing the appropriate catalyst for the OER can be guided by the rules explained in the previous section. An inspection of the volcano plot of the metal oxides with a ruthile structure suggest that a Co or Ni based oxide would be sufficient OER catalyst. However, practical application give rise to another

key performance parameter: stability. Although Co and Ni based catalysts are stable in alkaline pH, but tend to suffer from dissolution at neutral and acidic pH. IrO_2 catalysts are stable over the entire pH range and facilitate OER at low overpotential. Therefore, this catalyst is considered as benchmark for OER which has lead to vast amounts of data of using this material in literature.[12, 13, 14] Nevertheless, industrial applicability of this catalyst is hampered by its high costs since Ir is low abundant. Thus, research is directed towards the development highly stable OER catalysts composed of more abundant metals.[15, 16, 10, 17]

2.2.2 The oxygen evolution reaction in neutral environment

ECO2RR is predominantly performed in neutral pH. CO_2 dissolves to form less active bicarbonate and carbonate in alkaline conditions. Reduction of CO_2 in low pH faces competition of the hydrogen evolution reaction. Operating an electrochemical cell with electrolyte solutions of different pH at the anode and cathode raises the complexity and lowers the efficiency of an electrolyzer. Thus, finding a catalyst that performs the OER in neutral conditions is desirable. The design of a scalable system requires the catalyst to be highly stable and composed of affordable materials.[7] In this view, several reports been published. The characteristic properties of these systems are discussed in the following paragraphs.

Electrodeposited catalysts Some groups developed a strategy that involves the in-situ formation of an OER catalyst. In these studies, an inert electrode is placed in a phosphate buffered solution containing cobalt or nickel ions. A catalyst film containing metal oxides and phosphate anions forms when an oxidative potential is applied to the electrode. The in-situ formation of the catalysts implies a self-healing mechanism.[18, 19, 20] Other catalysts based on lithium cobalt oxides,[21] magnesium oxide [22, 23] and bismuth tungsten oxide [24] are also employed for OER in neutral media.

Brownmillerite catalysts Recently, Zhou et al. reported their discovery of a robust and highly active OER catalyst in neutral media.[7] their catalyst, Sr_2GaCoO_5 belongs to the class of Brownmillerite oxides, an oxygen-deficient derivative of perovskites. The properties of Brownmillerite oxides can be altered owning to their compositional degree of freedom. It has for instance been shown that doping the Ca cite of Ca_2MnAlO_5 with Ba and Sr lowers the equilibrium temperature for oxygen storage and release.[25] The reported high catalytic performance of Sr_2GaCoO_5 in comparison with IrO_2 forms the starting point of this project.
The authors attribute the high activity to the electron configuration that Co^{3+} adopts when it is encapsulated within the structure of the Brownmillerite oxide. Co is bound to four CoO_6 units and two GaO_4 units, resulting in Dh4 symmetry with intermediate spin as ground state, depicted in Figure 2.6. This configuration is believed to be to be crucial for the OER since the occupancy of the e_g symmetry electron approaches the theoretical optimum of about 1.2.[26] The prediction of high OER activity was supported with DFT calculations. Energy diagram for OER on Co-terminated (010) surface of Sr_2GaCoO_5 and Sr_2AlCoO_5 are plotted in Figure 2.6c. Theoretical overpotential calculated places both brownmillerite oxides at the top of the volcano plot for perovskites, Illustrated in Figure 2.5.

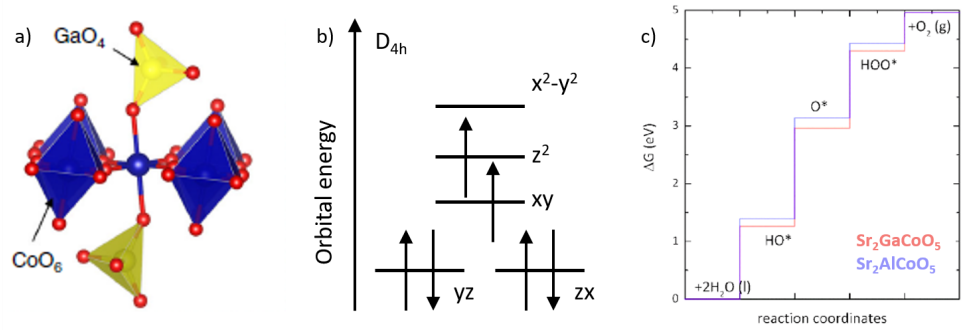

Figure 2.6: (a) Positioning of Co^{3+} within the Sr_2GaCoO_5 structure. (b) Electron configuration of Co^{3+} within the Sr_2GaCoO_5 structure. (c) Free energy diagrams for OER of Sr_2GaCoO_5 and Sr_2AlCoO_5. adopted from ref. [7].

Experimental

3.1 Materials

$SrCO_3$ (99.99%) and Co_3O_4 (99.99%) were purchased from Alfa Aesar. Ga_2O_3 (99%) was purchased from Sigma-Aldrich. $IrO_2 \cdot 2H_2O$ (99.99%) was purchased from Permion. NaH_2PO_4 (99%) was purchased from ARCOS organics. KOH, Na_2SO_4, 1,2-propanediol, and 1-propanol were purchased from Emsure. $KHCO_3$ and 3M KCl with AgCl were purchased from VWR chemicals. 1,2-propanediol (99.5% min) was purchased from ACS. MicroPolish^{TM} Alumina 0.3 and 1.0 µm were purchased from Buehler. TGP-H-090 Toray Paper 20% wet proofing was purchased from Fuel cell Earth. Vulcan XC-72R, Sigracet 39 BC, and D520 5% Nafion dispersion in propanol were purchased from Fuel Cell Store. Sustainion^{TM} XA-9 5 wt% in ethanol and Sustainion 4.7 wt% in 1,2 propanediol were purchased from Dioxide Materials. All chemicals were used as received.

3.2 Preparation of Sr_2GaCoO_5

The Sr_2GaCoO_5 catalyst powder was prepared according to the method described by Zhou et al.[7] Stochiometric amounts of $SrCO_3$, Ga_2O_3 and Co_3O_4 (42.6, 10.7, and 7.1 mmol respectively) with a combined mass of 10 g were ground together in an automatic mortar (FRITSCH Pulverisette 2) for 15 min. The light grey fine powder was transferred into an α-Aluminium container. The container was then placed into an oven and heated at a rate of 100 °C h^{-1} up to 1100 °C for 24 h. Thereafter, the sample was ground again and subjected to the same heat treatment for 216 h with two intermediate re-grinding steps after 48 h, and 144 h. The powder formed a solid dark grey slab after heat treatment that was ground into a fine powder with ease. The as synthesised product was ground carefully into a fine powder. A sample of ground powder was taken after each heat treatment.
A second batch of Sr_2GaCoO_5 catalyst powder was prepared with a slightly altered method. The combined mass of the starting compounds was 15 g. The powder was ground and subjected to the same heat treatment for only 120 h with one re-grinding step after 24 h. The powder was then ground with the automatic mortar for 40 min. Furthermore, 5 mL of MQ H_2O was added to the powder, this slurry was ground for 40 min. The water was evaporated in an oven at 90 °C overnight.
The first batch Sr_2GaCoO_5 was subjected to a sedimentation experiment. 700 mg was dispersed in 15 mL mQ H_2O and sonicated for 10 min with a Labsonic P sonicator (Sartorius). The suspension was left to settle down for 5 min after which 5 mL was taken from the top with a Finnpipepet. The obtained suspension was dried in an oven at 90 °C overnight.

3.3 Characterisation of Sr_2GaCoO_5 and IrO_2

3.3.1 X-ray diffraction

The starting compounds and all collected first batch Sr_2GaCoO_5 samples were studied with X-Ray diffraction (XRD). Typically 250-750 mg was used for analysis. The diffraction patterns were collected on an X'Pert PRO diffractometer from Malvern Panalytical, using a sealed tube with Cu anode as radiation source ($\lambda = 1.541874$ Å). The Scan range was 5–85° 2θ with a 0.0334° 2θ step size. The diffracted signals were recorded with an X'celerator multistrip detector giving an effective exposure time of 1000 s·$step^{-1}$. A programmable divergence slit ensured a fixed irradiated area of 10 x 10 mm.

3.3.2 N_2 physisorption

The specific surface areas of $IrO_2 \cdot 2H_2O$ and both batches Sr_2GaCoO_5 powders were determined with N_2 Physisorption measurements (3 Flex Micromeritics). Typically 1 g of sample was dried under vacuum at elevated temperatures for 16 h prior to the measurement. $IrO_2 \cdot 2H_2O$ was dried at 150 °C, the Sr_2GaCoO_5 samples at 350 °C. The surface areas were determined with a Brunauer-Emmett-Teller (BET) analysis.

3.3.3 Scanning electron microscopy

Roughly 20 mg of the catalyst powders were added to 4 mL 1-propanol. The obtained suspensions were sonicated for 10 min and drop-catsted onto carbon adhesive tabs with a 12 mm diameter (Electron Microscopy Sciences). This obtained with the sedimentation experiment was not sonicated prior to deposition on the SEM grid due to the little amount of available sample. The samples were analysed with a Tescan Vega II scanning electron microscope equipped with a thermo scientific detector. Images were taken at 10 and 20 kV with secondary electron imaging.

3.4 Electrochemical methods

The behavior of Sr_2GaCoO_5 as catalyst for OER was studied in comparison with IrO_2 as a catalyst. A cell with a rotating disk electrode and a half-cell were employed to study the behaviour of the catalysts. The preparation of the WE with the active material and the design of the setups are described in detail in the sections beneath.

3.4.1 Linear sweep voltammetry with the rotating disk electrode setup

The OER experiments with the rotating disk electrode were carried out in a three-electrode setup. A schematic design of this setup is shown in Figure 2.3. The RRDE Pt-GC (Pine Research) with catalyst film was employed as WE. An ink containing the catalyst was prepared by adding 4 mL MQ H_2O to 58 µM catalyst and 2.62 mg carbon black (Vulcan XC-72R). This suspension was sonicated for 10 min. Subsequently, 50 µl of 5 wt% nafion solution was added. The WE was polished prior to every experiment. First with a slurry of a few water droplets and 1.0 µm alumina for 2 min, thereafter with a slurry 0.3 µm Alumina powder for 2 min. Thereafter, 15 µl catalyst ink was drop-casted on the electrode with a Finnpipette. The solvent evaporated in air overnight to form a catalyst film.
Th rotating disk electrode setup was assembled with a 3 M Ag/AgCl RE, connected to the main compartment with a lugin capillary. The CE, a Pt coil was separated from the main compartment with a porous glass frit. The experiments were carried out at room temperature with an electrolyte composed of 0.4 M NaH_2PO_4 and 0.6 M Na_2SO_4 tuned to pH 7 with the appropriate amount of KOH (electrolyte pH 7). Linear sweep voltammograms were recorded with a scan rate of 1 $mV \cdot s^{-1}$. The potential was swept between 0 and 1.5 V vs Ag/AgCl for 5 times prior to every measurement.

3.4.2 Chronopotentiometry with the half-cell setup

The design of the half-cell setup can again be described as a three-electrode setup, the design together with a picture is shown in Figure 3.7. The WE was composed of a gas diffusion layer on which the catalyst of choice was deposited, two methods used for catalyst deposition are described in the following sections. A tiny 3 M Ag/AgCl electrode was used as a reference and Pt foil was used as CE. The platinum foil is placed in the center of a stainless steal (SS) cathode plate, with a ring shaped gasket around it. The foil and the gasket are sandwiched between the cathode plate and a plastic ring with a 2 cm^2 opening and an outer diameter equal to the cathode plate. A Teflon ring is then placed on top of the plastic ring and the assembly is placed on an open end of the glass cylinder. The anode side is prepared in an analogous manner with a Titania plate, an anode containing the OER catalyst, and a plastic ring with a 1 cm^2 opening. Hence, the cell is closed of leak tight. The RE is brought in the proximity of the WE via an additional opening in the wall of the cell. A stirring bean was placed in the cell to enable convection with a magnetic stirrer.
Chronopotentiometry experiments were performed at low currents and high currents. The low current experiments were conducted with 0.1 M $KHCO_3$ as electrolyte. The current was raised from 1 to 5 $mA \cdot cm^{-2}$ in five steps of 30 min. The high current experiments were conducted with electrolyte pH 7. In this series, The current was raised from 100 to 300 $mA \cdot cm^{-2}$ in five steps of 30 min. The potential was swept between 0 and 1.5 V vs Ag/AgCl for 5 times prior to every measurement.

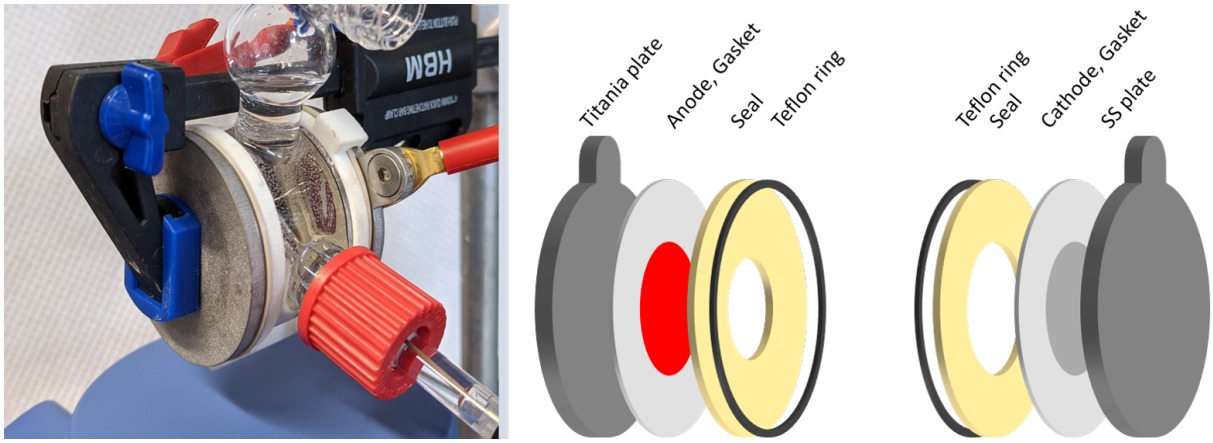

Figure 3.7: Photograph and schematic representation of the half-cell setup.

3.4.3 Preparation of the half-cell working electrodes: the spray paint method

$IrO_2 \cdot 2H_2O$ was deposited on a two graphite based gas diffusion electrodes (GDE) (grafite paper 39-BC (Sigracet) & TGP-H-090 Toray Paper 20% wet proofing (Fuel cell Earth)) with a spray-painter (TG Talon Gravity Feed Airbrush) illustrated in Figure 3.8a. A 3 by 6.7 cm GDE was dried at 90 °C for 30 min and placed on a vertically positioned heating plate heated at 30 °C. The GDE was fixated with a plastic sheet with a window of 3 by 6 cm. The spray-painter was placed into a holder at a distance of 10 cm of the GDE and connected to hose providing compressed air which was blown trough the system at 0.2 bar. The trigger of the spray painter was set into a fixed position with the aid of a rubber band. The painter was tuned to spray a spot of about 3 mm diameter. The heating plate with the GDE was programmed to move in a regular pattern in order to deposit an even layer of catalyst ink on the GDE. The spray-painter was filled with ink once the system was operational and the plate was moving. The GDE was dried at 90°C for 30 min after the deposition of the ink. The ink was prepared by combining 1.5 mL H_2O, 1.5 mL 2-propanol, 72 mg $IrO_2 \cdot 2H_2O$ and 36.8 µl 5 wt% sustainion solution in ethanol. The ink was sonicated for 10 min before use.

3.4.4 Preparation of the half-cell working electrodes: the bar coater method

The spray paint method appeared not to be valid for the preparation of a gas diffusion electrode with the Sr_2GaCoO_5 catalyst. The Sr_2GaCoO_5 clogged the spray painter as it was not divided finely enough. Hence, we used another method for electrode preparation termed the bar coater method. This method is illustrated in Figure 3.8b. Here 4 x 9 cm GDE sheets were used. An ink was prepared by combining 1 gram of catalyst with to 2 g 1,2-propanediol and 0.43 g 4.7 wt% sustaninion in 1,2-propanediol solution. This ink was sonicated for 10 min. Thereafter, line of 0.5 mL ink was applied to the top of the GDE which was fixated horizontally with adhesive tape. The bar coater, a rod with a screw thread like surface and a handle, was carefully placed on top of the ink, wobbled and swiftly drawn over the GDE while applying moderate pressure. As a result, the ink was evenly divided over the substrate. Hereafter the substrate was dried at 90°C for 15 min before applying another layer of ink. The electrode was ready for use after a repetition of the drying step.

3.4.5 X-ray fluorescence spectroscopy

The spent electrolytes of the half-cell experiments conducted with the Sr_2GaCoO_5 Toray electrodes with both low and high current were subjected to an elemental analysis with wavelength dispersive X-ray fluorescence (WD-XRF) spectroscopy. The measurements were quantified with a reference sample containing 10 $mg \cdot kg^{-1}$ of Ga, Co and Sr.

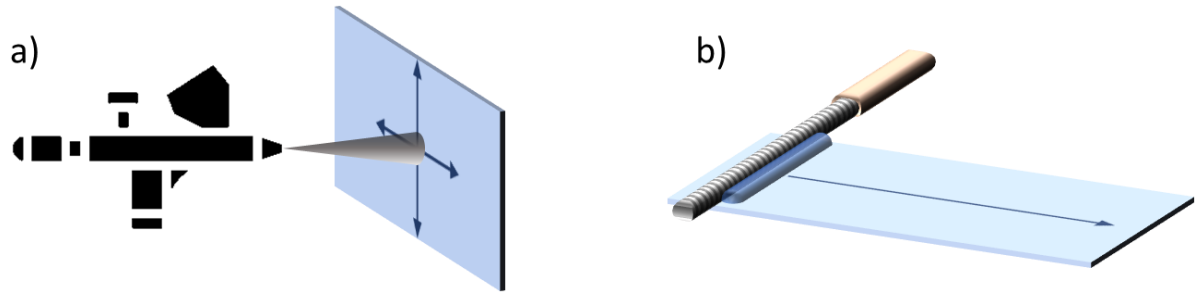

Figure 3.8: Schematic representation of (a) the the spray paint method and (b) the bar coater method.

3.4.6 Data processing

The potentials were corrected for the Ohmic drop caused by the resistance of the electrolyte. The resistance was measured with the current interrupt method. The potentials were measured versus a Ag/AgCl electrode with 3 M KCl. The potentials were corrected to the reference hydrogen electrode (RHE) as follows:

$$E(VvsRHE) = E(Ag/AgCl) + 0.207 + 0.059 * pH \tag{3.14}$$

Results and discussion

This chapter covers the results of the characterization of the Sr_2GaCoO_5 catalyst. Furthermore, the behaviour of the Sr_2GaCoO_5 catalyst in comparison with the benchmark IrO_2 catalyst is evaluated in several electrochemical experiments.

4.1 Characterization of Sr_2GaCoO_5 and IrO_2 catalysts

The Sr_2GaCoO_5 catalyst was prepared by subjecting a mixture of $SrCO_3$, Ga_2O_3 and Co_3O_4 to an extensive heat treatment at 1100 °C for 240 h. The heat treatment was interrupted three times for intermediate re-grinding with an automatic mortar after which a sample was collected. The synthesised product, the collected samples and the starting compounds where analysed with XRD in order to see if and when the crystalline phase of Sr_2GaCoO_5 formed. The normalised and base-line corrected diffractograms are shown together with the literature reference in Figure 4.9. $SrCO_3$ and Co_3O_4 appeared to be pure phases whereas the diffractogram of Ga_2O_3 shows signals that indicate the presence of oxyhydroxides in low quantities. The angle at which the most intense diffraction peaks of the starting compounds appeared are highlighted in the plot. One can clearly see that these reflections disappear, already after 24 h of heat-treatment. The new phase that arises does not change notably during further heat-treatment. Thus, the phase of the final product forms after 24 h.

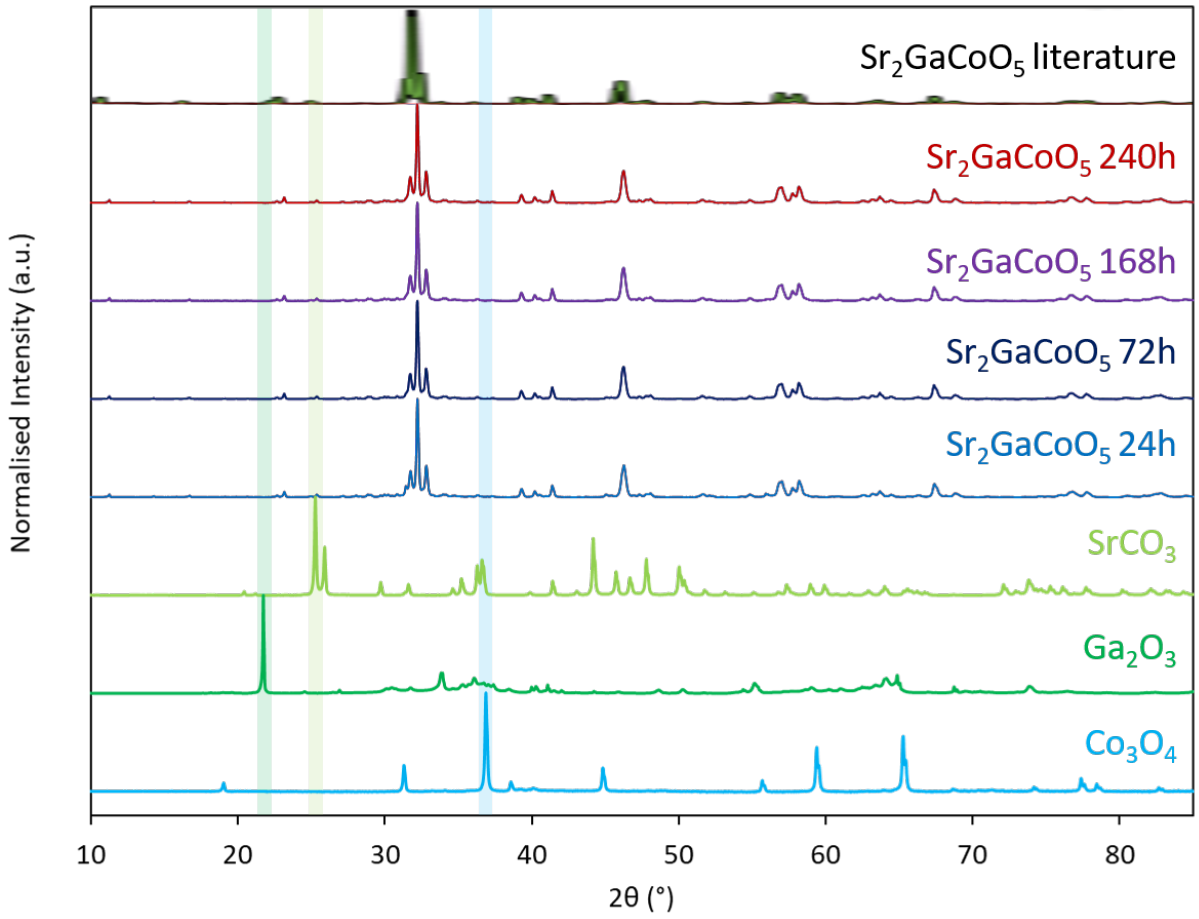

Figure 4.9: XRD results. The diffractograms of the starting compounds $SrCO_3$, Ga_2O_3, and Co_3O_4, the samples taken during the preparation of Sr_2GaCoO_5 and the literature reference adopted from ref. [7].

A reference diffractogram for Sr_2GaCoO_5 was not found in the database. In addition, the quality of the diffractogram reported in literature was not sufficient to be converted into a digital pattern for a thorough comparison. This leaves only a visual inspection of the observed pattern and the reference as a method to asses weather or not the Sr_2GaCoO_5 phase had formed. The high degree of resemblance between the diffractograms makes it highly likely that the preparation of Sr_2GaCoO_5 was successful.
XRD also offers the possibility to determine the size of the crystallites, with the Scherrer equation, since the broadening of the peaks is inversely proportional to the crystallite size. Authors of the article stated that the additional heat treatment leads to sintering of the crystals. The broadening of the strongest reflections of the Sr_2GaCoO_5 samples does however not change significantly over time. The average crystallite size was determined to be 85 nm for all Sr_2GaCoO_5 samples.

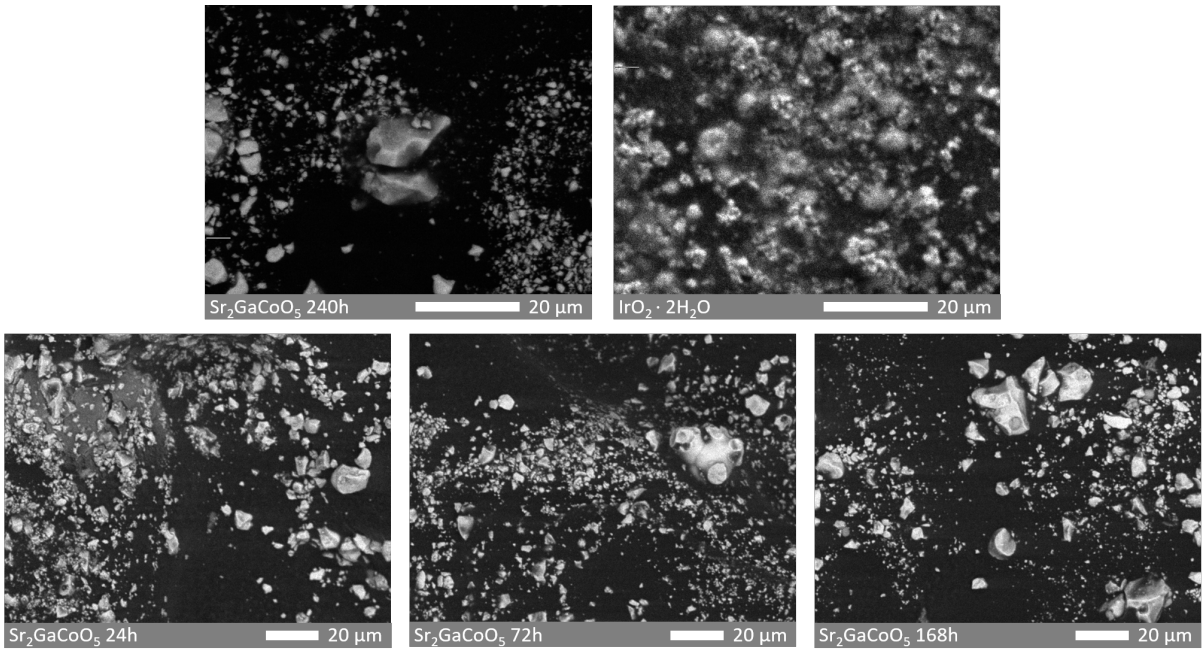

Figure 4.10: SEM images of the as synthesised Sr_2GaCoO_5 powder, the samples taken during catalyst preparation and IrO_2

The evolution of the morphology of the Sr_2GaCoO_5 powder was also monitored during the preparation process, in order to determine if sintering towards bigger particles appeared. The SEM images taken of the powders collected over time during the heat-treatment are shown together with an image of the benchmark IrO_2 catalyst in Figure 4.10. All four SEM images of Sr_2GaCoO_5 show a rather broad particle shape and size distribution with sizes ranging from 0.5 µm to crystals larger than 20 µm. No clear growth could be observed over time. The edges of the crystals seem to get better defined, but this could also be due to random variation in quality of the images. The IrO_2 image shows that this powder consists of spherical particles with sizes up to about 10 µm.
The onset potential of the Sr_2GaCoO_5 catalyst towards OER, discussed in section 4.2.1, was higher than reported by Zhou et al.[7] We suspected that this was due to the large crystals and broad particle size distribution. This hypothesis was tested with a sedimentation experiment and the subsequent preparation of a second batch Sr_2GaCoO_5 catalyst with shorter heat treatment and additional grinding steps. The second batch Sr_2GaCoO_5 catalyst was subjected to a shorter heat treatment since XRD analysis revealed that the desired phase formed after 24 h at 1100 °C. The SEM images of the second batch Sr_2GaCoO_5 catalyst before and after extensive grinding and an image of the sedimented Sr_2GaCoO_5 are shown in Figure 4.11. The SEM image of the second batch Sr_2GaCoO_5 resembles the images taken of the first batch Sr_2GaCoO_5, the image taken after more extensive grinding reveals the genesis of a powder composed of smaller and more spherical particles. In some cases, grinding can result in the formation of amorphous material or lead to phase change to another crystal structure. the observed crystals obtained with the sedimentation experiment are rather big, in contrast to our expectations. This particular sample was not sonicated prior to deposition on the SEM grid due to the little amount of available sample. Leaving out

the sonication step could have kept crystal agglomerates intact that would have fallen apart otherwise.
The activity of a catalyst is commonly corrected for its surface area in order to make a fair comparison

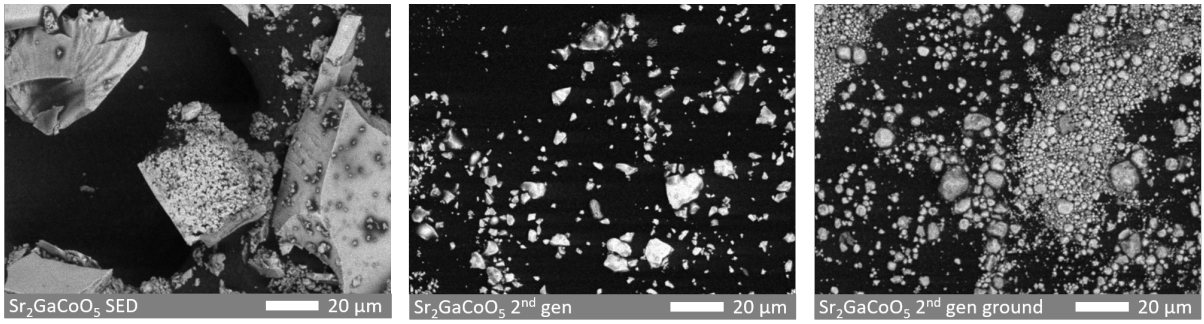

Figure 4.11: SEM images of the second batch Sr_2GaCoO_5 powder before and after extensive grinding and an image of the sample taken of the powder obtained after the sedimentation experiment

between different materials. Therefore, the Sr_2GaCoO_5 and IrO_2 powders were analysed with N_2 physisorption. The BET surface areas where determined to be 5.31 and 30.24 m^2g^{-1} respectively. The BET surface area of the second batch Sr_2GaCoO_5 catalyst was 23.17 m^2g^{-1}. The increased area indicates that the shorter heat-treatment and the extensive grinding resulted in the generation of smaller Sr_2GaCoO_5 particles and hence a larger specific surface area.

4.2 Electrochemical tests

Electrochemical performance of Sr_2GaCoO_5 in the OER reaction in comparison with IrO_2 was evaluated with linear sweep voltammetry (LSV) and chronopotentiometry (CPOT). The first technique was employed to determine the activity towards OER of both catalyst. The second technique was used to study the stability of the catalysts in an system that resembles an electrolyzer.

4.2.1 Activity assessment with linear sweep voltammetry

The activity of the Sr_2GaCoO_5 catalyst was experimentally compared with the benchmark IrO_2 catalyst with LSV. Here, the potential is externally changed at a constant rate. The resulting flow of current is followed as function of applied potential. The steadily increasing oxidising potential will eventually be high enough to facilitate OER, indicated by the flow of current. This point, the so called onset potential, is a key indicator for catalytic activity. A good catalyst facilitates OER at low potentials.
The LSV experiments were conducted in a typical three-electrode setup with a glassy carbon rotating disk electrode equipped with a catalyst film as WE. First, IrO_2 and Sr_2GaCoO_5 were tested with an electrolyte of 0.4 M NaH_2PO_4 and 0.6 M Na_2SO_4 tuned to pH 7 with the appropriate amount of KOH to mimic the experiment conducted by Zhou et al. The results of these test, corrected for the resistance of the solution and converted to current per BET surface area, are shown, together with the literature reference, in Figure 4.12a. The IrO_2 benchmark shows lower onset potential than reported. More important is the observation that the Sr_2GaCoO_5 catalyst is not as active as portrayed. In addition, the current rises rather slow with rising potential.
We suspected that the poor activity slow rise of current was the result of the rather big Sr_2GaCoO_5 crystals and small specific surface area compared to the catalyst used by Zhou et al. This study reports a surface area of 8.4 m^2g^{-1} whereas our had 5.31 m^2g^{-1}. The recipe of the ink was adopted from Zou et al, thus the same amount of ionomer was used with a catalyst with a smaller surface area. Therefore, the ink possessed a higher ionomer/catalyst surface area ratio. As an effect, the ionomer could have covered most of the catalyst crystals, lowering the amount of active sites, and as a result the flow of current. We tested this hypothesis by varying the amount of ionomer in the ink, with half and double the amount as was used originally, indicated with 0.5N and 2N. In addition, we aimed to remove some of the larger crystal chunks from the catalyst powder with a sedimentation experiment. The obtained powder was

also processed in an ink and subjected to a catalytic test. The results of these experiments are depicted in Figure 4.12b. The current in this plot was not corrected for the specific surface area as the amount of catalyst obtained with the sedimentation experiment was not sufficient to perform a BET analysis.
The linear sweep voltammograms depicted in Figure 4.12b illustrate that the amount of ionomer does not change the onset potential to a large extent. However, the rise of current is effected. Doubling the amount of ionomer results in a flatter line. This indicates a decrease in active sites. Less ionomer results in a steeper curve, indicative for an increased amount of active sites. The electrochemical experiment with the sediment catalyst shows lower onset potential and steep current increase. We ascribe the improved performance to the removal of the big crystal chunks.

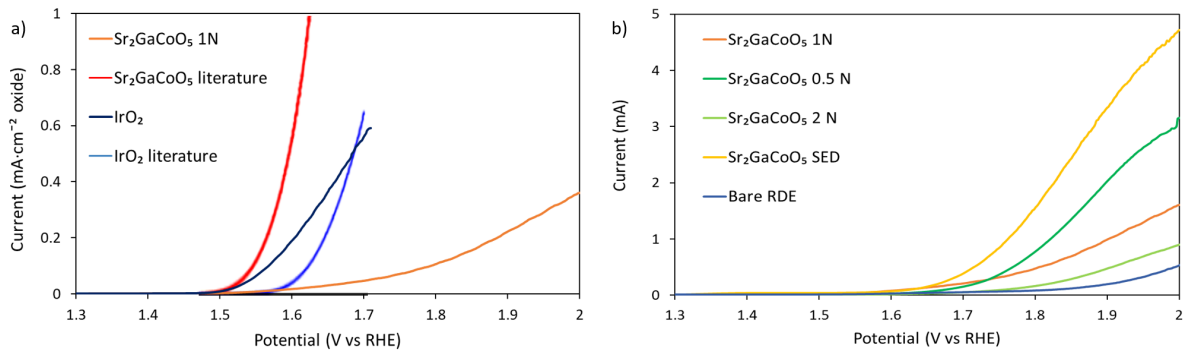

Figure 4.12: Linear sweep voltammograms obtained with the RDE setup with the pH 7 electrolyte. (a) The current corrected for the BET surface area of the catalyst is plotted against the potential vs RHE corrected for the Ohmic drop of the solution. Both experimentally obtained results and the results reported by Zhou et al are shown. (b) The current vs the potential vs RHE corrected for the Ohmic drop of the solution.

The results of this second set of experiments urged us to prepare a second batch Sr_2GaCoO_5 with smaller crystals, with a shorter heat treatment and extensive grinding. Again, this catalyst was processed in an ink and applied to the rotating disk electrode. The influence of the ionomer was studied analogous to the previous experiments. The activity towards OER of this second batch is illustrated and compared with the previous experiments, illustrated with Figure 4.13a. The second batch shows both a higher onset potential and a flatter curve for all studied ionomer/catalyst ratios. The extensive grinding might have resulted in the formation of amorphous material or a phase change to another crystal structure. Either way, the second batch Sr_2GaCoO_5 is less active than the first.
The key results of the LSV experiments are summarised and quantified in Figure 4.13b. Here, the overpotential required to generate a current flow of 20, 50 and 100 $\mu A \cdot cm^{-2}$ is shown in comparison to the results reported by Zhou et al. The lowest achieved overpotential at 20 $\mu A \cdot cm^{-2}$, of Sr_2GaCoO_5 1N is 382 mV, 102 mV higher, than reported. The lowest achieved overpotential at 100 $\mu A \cdot cm^{-2}$, of Sr_2GaCoO_5 0.5N is 531 mV, 211 mV higher than reported. The benchmark, IrO_2 achieved an overpotential of 288 mV at 20 $\mu A \cdot cm^{-2}$. indicating that, at low current the difference between the benchmark and Sr_2GaCoO_5 is 94 mV, this gap increases with increasing current.

4.2.2 Stability assessment with chronopotentiometry

The stability of Sr_2GaCoO_5 in comparison with IrO_2 was assessed with CPOT. This is an electrochemical technique in which the current of the WE is set at a constant magnitude. The resulting potential required for the Faradaic processes occurring at the electrode is monitored as function of time. The experiments are conducted in a half-cell described in Figure 3.7. The WE's are prepared with two deposition techniques, with the spray painter for IrO_2 and bar coater for Sr_2GaCoO_5 with two substrates Toray (T) and Sigracet (S).
A series of CPOT experiments was performed at low current with a 0.1 M $KHCO_3$ electrolyte, to work in the activation controlled regime and minimize mass transport effects and the influence of the resistance of the electrolyte solution. The results of this study are shown in Figure 4.14a. The anodes prepared

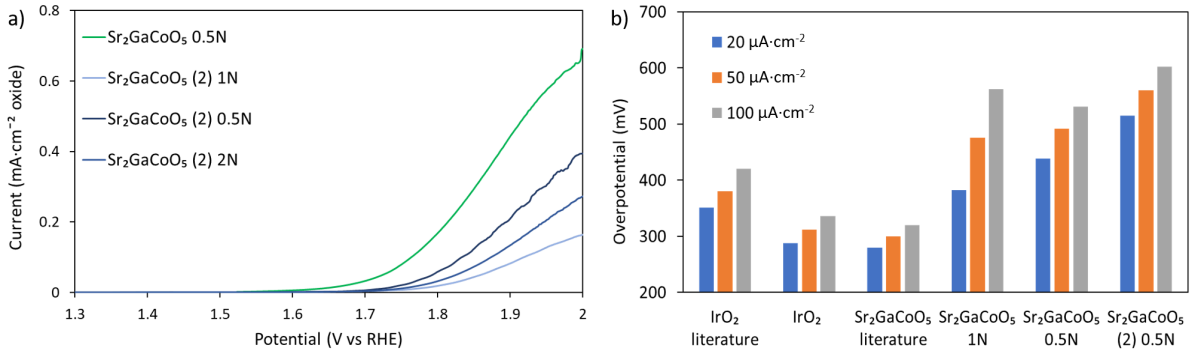

Figure 4.13: (a) Linear sweep voltammograms obtained with the RDE setup with the pH 7 electrolyte and the second batch Sr_2GaCoO_5 catalyst, in comparison with the first batch. The current corrected for the BET surface area of the catalyst is plotted against the potential vs RHE corrected for the Ohmic drop of the solution. (b) OER Overpotential at several current densities

with the IrO_2 catalyst appeared to facilitate OER at low overpotential. The IrO_2 based anodes were stable as the potential required to achieve the set current densities remained constant over time. The anodes prepared with the Sr_2GaCoO_5 catalyst require a higher potential to facilitate OER. The T anode showed week signs of degradation whereas the S electrode appeared to degrade during every current step. Therefore, we utilised T substrates in the next set of experiments.
The Other set of experiments, of which the results are shown in Figure 4.14b, was performed with higher currents ranging from 100 up to 300 $mA{\cdot}cm^{-2}$. These current steps where chosen since a CO_2 electrolyzer is required to draw a current of at least 250 $mA{\cdot}cm^{-2}$ in order to be economically feasible (source). Therefore it can be argued that a catalyst that requires a relatively low potential to facilitate OER, and proves to be stable in this experiment, can potentially be used in a CO_2 electrolyzer. The IrO_2 is highly stable as the potential required to draw the set current is practically constant. Furthermore, the potential required is low: between 2.5 and 3 V vs RHE. These observations illustrate that the spray paint technique is suitable for the preparation of a highly stable IrO_2 based anode.
Electrodes prepared with both batches of Sr_2GaCoO_5 catalyst behaved different. Extensive degradation is illustrated by the increasing potential in the 100 $mA{\cdot}cm^{-2}$ step. Even faster degradation sets in when the current is set at 150 $mA{\cdot}cm^{-2}$, the potential surpasses a critical border of 6 V vs RHE quickly, the experiments were stopped after this point to prevent decomposition of the carbon substrates and damage to the cell. These results clearly show that the current batches of Sr_2GaCoO_5 catalyst are not suitable to compete with the IrO_2 catalyst.

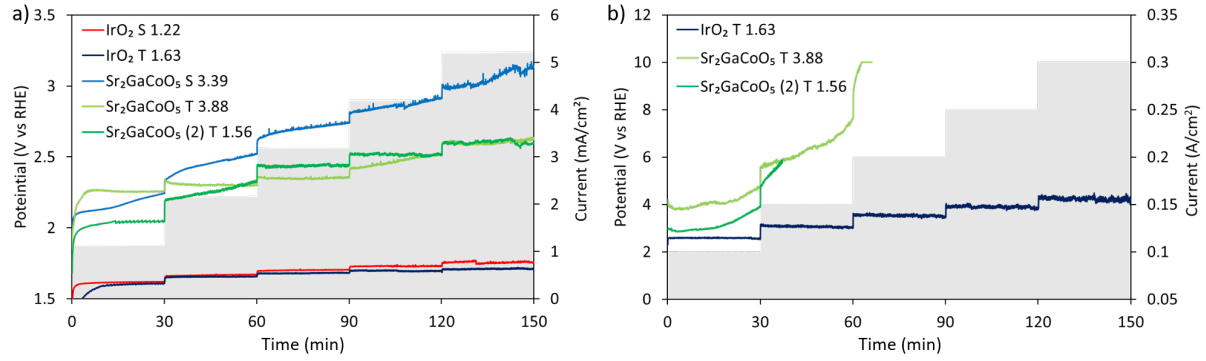

Figure 4.14: Chronopotentiometry results. (a) Experiments conducted at low current in 0.1 M $KHCO_3$ and (b) at high current in pH 7 electrolyte. The current steps are illustrated with they grey areas in the plots. Only the results of the experiments conducted at low current are corrected for the Ohmic drop of the solution. The loading of catalyst on the Sigracet (S) or Toray (T) substrates are shown in $mg{\cdot}cm^{-2}$

The origin of the degradation phenomena observed for the Sr_2GaCoO_5 based anodes was studied with WD-XRF. The spent electrolytes of both half-cell experiments conducted with the first batch Sr_2GaCoO_5 Toray electrodes were analysed. The results of are shown in Table 4.1. Significant amounts of catalyst material were found in the spent electrolytes, indicating the leaching of catalyst material from the GDE a major degradation pathway.

Table 4.1: Elemental analysis with WD-XRF of the spent electrolytes collected after the half-cell experiments conducted with the first batch Sr_2GaCoO_5 catalyst.

Sample	Sr ($mg \cdot kg^{-1}$)	Ga ($mg \cdot kg^{-1}$)	Co ($mg \cdot kg^{-1}$)
Sr_2GaCoO_5 T low current	n.a.	5	n.a.
Sr_2GaCoO_5 T high current	25	43	35

Conclusions

We made an effort to enhance of the cost efficiency of the anodic side of a CO_2 electrolyzer. Our strategy to do so involved the replacement the benchmark IrO_2 OER catalyst with a more active catalyst composed of abundant materials that facilitates OER at neutral pH. In this view, our attention was drawn to an article published by Zhou et al. The authors reported Sr_2GaCoO_5 as a highly stable catalyst that facilitated OER at lower potentials than the benchmark IrO_2. We aimed to reproduce these results. XRD analysis of the samples taken during the preparation process of Sr_2GaCoO_5 revealed that phase of the final product forms after 24 h of heat treatment. The high degree of resemblance between the reported diffractogram and the recorded diffractogram of the final product makes it highly likely that the preparation of Sr_2GaCoO_5 was successful. The evolution of the morphology of the Sr_2GaCoO_5 powder over time during heat treatment was monitored with SEM. All SEM images showed a rather broad particle shape and size distribution with sizes ranging from 0.5 µm to crystals larger than 20 µm. No clear particle growth could be observed over time. The second batch Sr_2GaCoO_5 prepared with a shorter heat treatment and additional grinding steps was composed of smaller and more spherical particles. The BET surface areas of Sr_2GaCoO_5 (batch 1), Sr_2GaCoO_5 (batch 2) and IrO_2 where determined to be 5.31, 23.17 and 30.24 m^2g^{-1} respectively. Indicating that the adaptation of the preparation method yielded a powder with a larger specific surface area.

The activity of Sr_2GaCoO_5 in comparison with IrO_2 was evaluated with LSV. Sr_2GaCoO_5 facilitated OER with an overpotential of 382 V at 20 µA·cm^{-2}, the IrO_2 catalyst exhibited an overpotential of 288 mV at the same current. The potential gap between the two catalysts increased further with rising current. The Sr_2GaCoO_5 catalyst was reported to require an overpotential of only 280 mV to facilitate OER at 20 µA·cm^{-2}. The second batch Sr_2GaCoO_5 appeared to be less active than the first. This observation was attributed to the longer grinding steps that might have caused the formation of amorphous less active material.

The stability of the catalysts was studied with CPOT in neutral pH, under high current conditions that can applied in a CO_2 electrolyzer. The IrO_2 anode appeared to be highly stable and only required a potential between 2.5 and 3 V vs RHE to facilitate OER at current density's ranging from 100 up to 300 mA·cm^{-2}. The Sr_2GaCoO_5 based catalyst showed severe signs of degradation under the same conditions. The degradation was attributed to leaching detected with WD-XRF.

The low intrinsic activity, observed with LSV, and instability, detected with CPOT, of the Sr_2GaCoO_5 catalyst diminishes its applicability in a CO_2 electrolyzer. Such a system is required to run at low constant potentials with constant current in order to make it feasible. The experiments conducted with IrO_2 sowed that this material was both more stable and more active. Furthermore, A CO_2 electrolyser equipped with IrO_2 as anode material is reported to run with a constant current density for up to 18 h.[14]. Therefore, the replacement of the benchmark IrO_2 catalyst by Sr_2GaCoO_5 is not a valid strategy to enhance the performance of the CO_2 electrolyzer.

Outlook

6.1 Alternative oxidation reactions in a CO_2 electrolyzer: partial methanol oxidation

Recently, more attention is directed towards electrochemical reactions that occur on the anode of a CO_2 electrolyzer. Motivation for this effort originates from the economical need to improve the energy efficiency of the system. Typically, ECO2RR is coupled with OER. The latter reaction is kinetically sluggish and lays a heavy burden on the efficiency of the electrolyzer. Approximately 90% of the electricity input is consumed by the OER when reduction of CO_2 to CO is considered.[6] Thus, finding an oxidation reaction that requires less energy can increase the feasibility of an integrated ECO2RR system considerably. In addition, electrochemical oxidation can provide an alternative pathway towards value added feedstock.
Several considerations should be made when it comes to the selection of proper feed for an alternative oxidation reaction at the anode of a CO_2 electrolyzer. The production of the feed aught not to be energy intensive and result in CO_2 emissions. Furthermore, the oxidation reaction must be scalable with ECO2RR. In addition, the costs of the feedstock should be low, and the oxidized compound should posses added value.[27, 28, 6] In this view, a techno-economic analysis within Shell was performed for a list of oxidation reactions. Promising feedstock and products where compared with the chemical portfolio of Shell. This resulted in a list of economically feasible alternative oxidation reactions, listed in Table 6.2. The first three reactions are explored at the technology center in Amsterdam. The reactions beneath the double horizontal line are studied in the technology center in Bangalore. The major feedstock of the first three reactions is methanol. Hence, we subjected the partial electrochemical oxidation of methanol towards dimethyl carbonate, (DMC) mono-ethylene glycol (MEG) and, formaldehyde to a literature review. The following paragraphs cover literature on the partial oxidation of methanol towards DMC, formaldehyde and MEG.

Table 6.2: Potential oxidation reactions as alternative to OER. The chemical target and the electrochemical half-reaction. Reactions beneath the double horizontal line are studied at the Shell Technology Center Bangalore, reactions above the double horizontal line are investigated at Shell Technology Center Amsterdam.

Catalyst	**Electrolyte**
Dimethyl carbonate (DMC)	2 methanol + CO $\longrightarrow$ DMC + 2 e^- + 2 H^+
Mono ethylene glycol (MEG)	2 methanol $\longrightarrow$ MEG + 2 e^- + 2 H^+
Formaldehyde	methanol $\longrightarrow$ CH2O + 2 e^- + 2 H^+
Hydrogen peroxide (H_2O_2)	2 H_2O $\longrightarrow$ H_2O_2 + 2 e^- + 2 H^+
Phenol (PhOH)	C_6H_6 + H_2O $\longrightarrow$ PhOH + 2 e^- + 2 H^+
Propylene oxide (PO)	C_3H_6 + H_2O $\longrightarrow$ PO + 2 e^- + 2 H^+
Propylene glycol (PG)	C_3H_6 + 2 H_2O $\longrightarrow$ PG + 2 e^- + 2 H^+

6.1.1 Methanol oxidation towards formaldehyde

Formaldehyde is a gas that is industrially prepared via the dehydrogenation of methanol with the aid of a silver-based catalyst. The compound is used in chemical industry as feedstock for the production of other chemicals. As an alternative to the industrial route, methanol can by oxidized to yield formaldehyde. Only a few reports describe partial methanol oxidation towards formaldehyde in solution at moderate temperatures.
The anode material of choice to partially oxidize methanol in an aqueous solution towards formaldehyde was Pt.[29, 30] Dissociative methanol adsorption occurs readily on Pt but the side product CO act as a poison to the surface. Formaldehyde formed between 0.2 and 0.6 V vs Ag/AgCl with a maximal yield of 38%. Increasing the potential further resulted in methanol decomposition to CO_2. Formaldehyde yield falls below 2% on carbon supported catalysts in Nafion. Authors suspect that this was the result

of complete methanol oxidation facilitated by the array of active sites within the Nafion film. Both the reaction of methanol to formaldehyde and the key results of a study concerning this reaction are depicted in Figure 6.15.

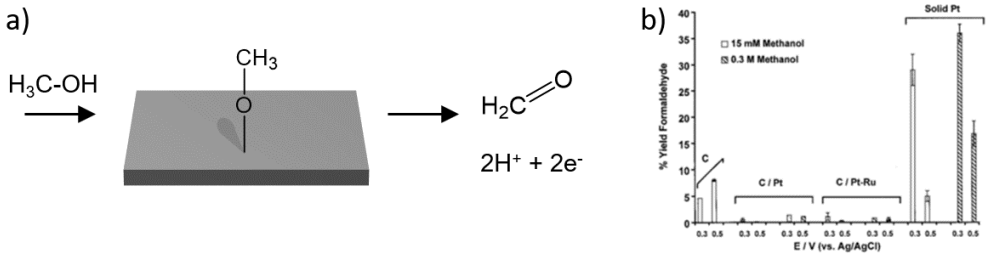

Figure 6.15: (a) Oxidation of methanol to formaldehyde over an anodic surface. (b) Formaldehyde yield versus applied potential and applied anode material. Adopted from ref. [30].

6.1.2 Methanol oxidation towards mono ethylene glycol

MEG or ethane-1,2-diol is is mainly used as building block for polyester fibers and for antifreeze applications. To the best of our knowledge there is no literature on direct electrochemical oxidation of methanol to form MEG. However, formaldehyde can be synthesized starting from methanol via the electrochemical pathway described above. Subsequently, formaldehyde can be electrochemically converted to form MEG with the aid of a carbon-based cathode. Thus, providing a strategy to couple the two carbon atoms of methanol with the aid of electrical power.[31, 32] This process however requires the reduction of formaldehyde at the cathode of an electrochemical cell, which is in conflict with the aim of this study that focuses on oxidation reactions that can be paired with ECO2RR.

6.1.3 Methanol oxidation towards dimethyl carbonate

DMC is a low toxic biodegradable chemical building block that is applied in various synthesis reactions, as fuel additive and a polar solvent. In industry, DMC is synthesized based on oxidative carbonylation. High demand has driven the development of new methods that use green energy and produce less waste. The academic interest for the electrochemical synthesis of DMC originates from the beginning of this century. Pioneering experimental work has been done by a Japanese group.[33, 34, 35] The first report by this group concerns the optimization of the reaction conditions for DMC synthesis with a Pd based electrode.[35] In this report the composition and concentration of electrolyte, partial pressure of CO and, anode potential are tuned to an optimum. Methanol containing 0.1 M $NaClO_4$ electrolyte was most suitable. The second report of the group on DMC synthesis concern a study on product selectivity with a similar system employed with a Au based anode.
In both reports, a H-type electrolysis cell was assembled with a Pd or Au based anode and Pt-based cathode. These electrodes where prepared with the so-called hot-press method. The electrocatalyst, vapor-growing carbon fiber (VGCF) supported Pd or Pt are combined with Teflon powder and pressed and shaped into a round wafer on a hot plate (393K).
Liquid samples were periodically withdrawn and analyzed with chromatography to study product formation. The reported products in the liquid phase were DMC, dimethyl oxalate (DMO) dimethoxymethane (DMM), and methyl formate (MF). The gas outlet of the cell was monitored with online chromatography to quantify CO_2 production. The key results of these studies are shown in Figure 6.16. The selectivity towards DMC was reported to be 59% and 3% at 1 V vs Ag/AgCl for Pd and Au respectively. In these conditions the use of the Au electrode yielded 30% DMO. It was found that the product distribution could be shifted dramatically towards DMC, up to 80% (as fraction of the total amount DMC and DMO) by increasing the applied potential.[34, 33]

The mechanism of electrochemical DMC synthesis has been investigated recently by means of in-situ spectroscopy and DFT calculations.[36, 37] The initial step is assumed to be the adsorption of CO. This

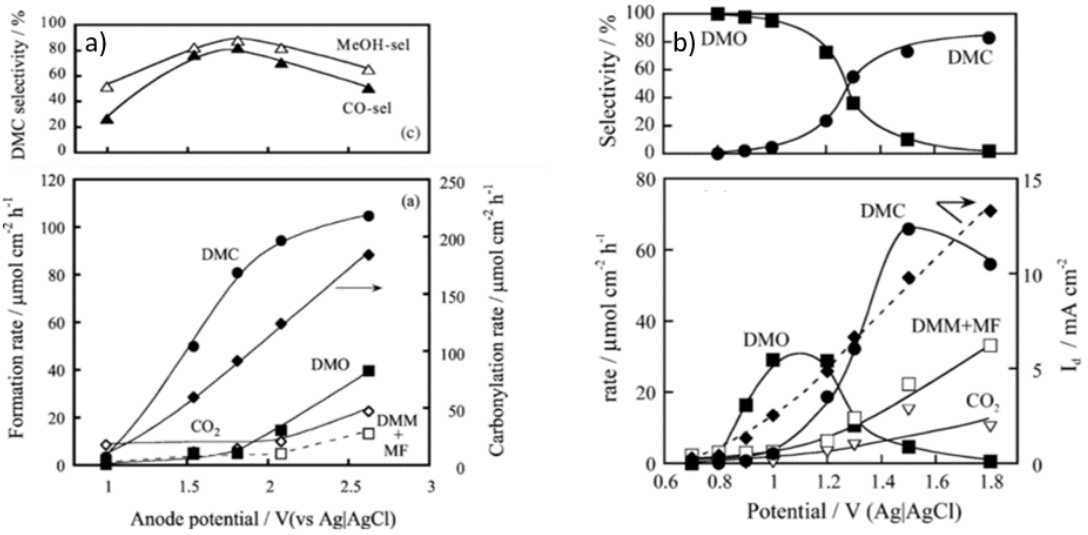

Figure 6.16: Effects of anode potential on the DMC formation rate over supported Pd (a) and Au (b) anodes and the DMC selectivity. T = 298 K, 101 kPa CO, 0.1M $NaClO_4$ in methanol. Reproduced from ref. [35] and ref. [34].

step is followed by the electrochemical activation of methanol, either via direct adsorption as methoxy, or by co-absorbing with CO to form adsorbed methyl formate. DMC is formed when two methoxy species combine with CO. DMO forms as a side product when two methyl formate species meet. Both routes for methanol activation involve a proton coupled electron transfer. Hence, the free energy of these steps can be lowered by applying a potential. The potential controlled selectivity towards DMO or DMC of gold based catalysts was theoretically explained by Saric et al. It was argued that Sufficient adsorption of methoxy groups resulting in the formation of DMC requires higher potential than adsorption of methyl formate which results in the formation of DMO.
DMC formation requires moderate absorption of both CO and methanol. When CO binds too strong with the metal, its surface is poisoned, and DMC formation is inhibited which is the case with Pt. On Ag DMC is also not formed as Ag does not absorb CO and binds methanol to strong. Pd and Au have moderated absorption energies for both compounds allowing absorption and preventing poisoning.
Residual amounts of water allow the formation of the side product methyl formate. In aqueous solution, the methoxy intermediate is oxidized to form formaldehyde that is hydrated and further oxidised to formic acid. The Formic acid subsequently reacts with methanol to form methyl formate. DMM can be produced as a result of methanol oxidation.

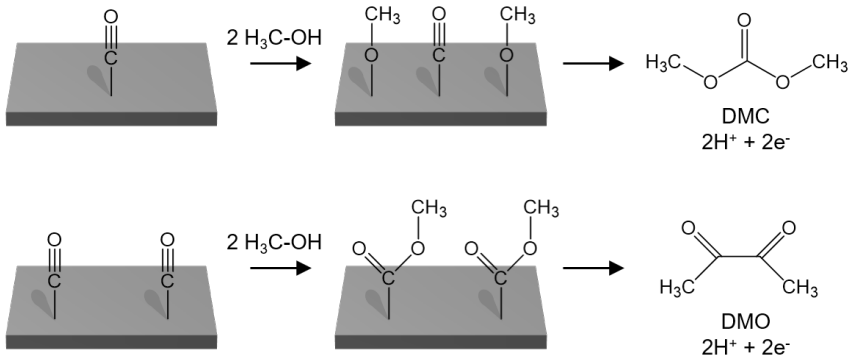

Figure 6.17: Methanol carbonylation via methoxy adsorption to form DMC, and via co-absorbing with CO to form adsorbed methyl formate to form DMO. reproduced from ref. [37].

6.1.4 Concluding remarks

Methanol can be partially oxidized to formaldehyde with the aid of a Pt based electrode. However, low yields and complete methanol oxidation to CO_2 are the major obstacles for this particular synthesis. Furthermore, direct electrochemical synthesis of MEG from methanol is not reported. With these considerations in mind, further exploration of electrochemical carbonylation of methanol to DMC is of major interest. Small scale proof of concept experiments with a half-cell equipped with a Pd based anode can be performed in order to reproduce the results reported by Yamanaka et al. [35] The data collected in these experiments such as the conversion of CO and selectivity towards DMC can be used in a more detailed study. A techno-economic analysis can reveal weather or not the coupling of ECO2RR and electrochemical methanol carbonylation towards DMC has the potential to be economically feasible.

Acknowledgements

I thank Paul Corbett as team lead and Esther van Soest-Vercammen as line manager for providing the opportunity to do this internship at the E-lab of the Shell Technology Center in Amsterdam. The past six months formed an engaging concluding part of the Masters Nanomaterials Science from Utrecht University. I thank Paul Corbett for his guidance throughout the project and his review of this report. His flexibility and creativity during the challenging times of the Corona pandemic made my time in lockdown well spent.
I thank Michiel de Heer for his daily supervision in the lab and his kind introduction in the wonder wold of electrochemistry. His training on electrode preparation and the use of electrochemical setups were essential for the experimental work. I thank Maarten Schellekens as member of the e-team for the advice and support he provided in the lab. I thank Sumit Verma for his input during ideation and review sessions.
I thank Prof. Petra E. de Jongh as first examiner for reviewing this report.
I thank Mickey Rietbergen for the SEM measurements. I thank Huub Kooijman for the XRD measurements. I thank Simon Papa and Alice van Velthuijsen for the N_2 physisorption measurements. I thank Ted Schroder for WD-XRF measurements.

Bibliography

[1] R. K. Pachauri and L. A. Meyer. Climate Change 2014 Synthesis Report. Technical report, 2014.

[2] S. Nitopi, E. Bertheussen, S. B. Scott, X. Liu, A. K. Engstfeld, S. Horch, B. Seger, I. E. L. Stephens, K. Chan, C. Hahn, J. K. Norskov, T. F. Jaramillo, and I. Chorkendorff. Progress and perspectives of electrochemical CO_2 reduction on copper in aqueous electrolyte. *Chem. Rev.*, 119(12):7610–7672, 2019.

[3] Y. Y. Birdja, E. Pérez-Gallent, M. C. Figueiredo, A. J. Göttle, F. Calle-Vallejo, and M. T. M. Koper. Advances and challenges in understanding the electrocatalytic conversion of carbon dioxide to fuels. *Nat. Energy*, 4(9):732–745, 2019.

[4] J. Qiao, Y. Liu, F. Hong, and J. Zhang. A review of catalysts for the electroreduction of carbon dioxide to produce low-carbon fuels. *Chem. Soc. Rev.*, 43(2):631–75, 2014.

[5] M. Gong and H. Dai. A mini review on NiFe-based materials as highly active oxygen evolution reaction electrocatalysts. *Nano Res.*, 8:23–29, 2015.

[6] S. Verma, S. Lu, and P. J. A. Kenis. Co-electrolysis of CO_2 and glycerol as a pathway to carbon chemicals with improved technoeconomics due to low electricity consumption. *Nat. Energy*, 4(6):466–474, 2019.

[7] L. Q. Zhou, C. Ling, H. Zhou, X. Wang, J. Liao, G. K. Reddy, L. Deng, T. C. Peck, R. Zhang, M. S. Whittingham, C. Wang, C. W. Chu, Y. Yao, and H. Jia. A high-performance oxygen evolution catalyst in neutral-pH for sunlight-driven CO_2 reduction. *Nat. Commun.*, 10(1):4081, 2019.

[8] D. W. Ball. *Physical Chemistry*. CENGAGE Learning, 1 edition, 2003.

[9] E Gileadi. *Physical Electrochemistry*. Wiley-VCH, 3 edition, 2015.

[10] J. S. Kim, B. Kim, H. Kim, and K. Kang. Recent progress on multimetal oxide catalysts for the oxygen evolution reaction. *Adv. Energy Mater.*, 8(11):1702774, 2018.

[11] I. C. Man, H. Y. Su, F. Calle-Vallejo, H. A. Hansen, J. I. Martínez, N. G. Inoglu, J. Kitchin, T. F. Jaramillo, J. K. Nørskov, and J. Rossmeisl. Universality in oxygen evolution electrocatalysis on oxide surfaces. *ChemCatChem*, 3(7):1159–1165, 2011.

[12] S. Cherevko, S. Geiger, O. Kasian, N. Kulyk, J. P. Grote, A. Savan, B. S. Ratna, S. Merzlikin, B. Breitbach, A. Ludwig, and K. J. J. Mayrhofer. Oxygen and hydrogen evolution reactions on Ru, RuO_2, Ir, and IrO_2 thin film electrodes in acidic and alkaline electrolytes: A comparative study on activity and stability. *Catal. Today*, 262:170–180, 2016.

[13] C. C. L. McCrory, S. Jung, J. C. Peters, and T.F. Jaramillo. Benchmarking heterogeneous electrocatalysts for the oxygen evolution reaction. *J. Am. Chem. Soc.*, 135:16977–16987, 2013.

[14] M. Schreier, L. Curvat, F. Giordano, L. Steier, Abate A., S. M. Zakeeruddin, J. Luo, M. T. Mayer, and M. Gratzel. Efficient photosynthesis of carbon monoxide from CO_2 using perovskite photovoltaics. *Nat. Commun.*, 6:7326, 2015.

[15] M. I. Jamesh and X. Sun. Recent progress on earth abundant electrocatalysts for oxygen evolution reaction in alkaline medium to achieve efficient water splitting – a review. *J. Power Sources*, 400:31–68, 2018.

[16] N. T. Suen, S. F. Hung, Q. Quan, N. Zhang, Y. J. Xu, and H. M. Chen. Electrocatalysis for the oxygen evolution reaction: recent development and future perspectives. *Chem. Soc. Rev.*, 46(2):337–365, 2017.

[17] M. Tahir, L. Pan, F. Idrees, X. Zhang, L. Wang, J. J. Zou, and Z. L. Wang. Electrocatalytic oxygen evolution reaction for energy conversion and storage: A comprehensive review. *Nano Energy*, 37:136–157, 2017.

[18] Y. Surendranath, M. Dinca, and D. G. Nocera. Electrolyte-dependent electrosynthesis and activity of cobalt-based water oxidation catalysts. *J. Am. Chem. Soc.*, 131:2615–2620, 2009.

[19] M. W. Kanan and D. G. Nocera. In situ formation of an oxygen-evolving catalyst in neutral water containing phosphate and Co^{2+}. *Science*, 321:1072–1075, 2008.

[20] M. Dinca, Y. Surendranath, and D. G. Nocera. Nickel-borate oxygen-evolving catalyst that functions under benign conditions. *PNAS USA*, 107(23):10337–41, 2010.

[21] G. Gardner, J. Al-Sharab, N. Danilovic, Y. B. Go, K. Ayers, M. Greenblatt, and C. G. Dismukes. Structural basis for differing electrocatalytic water oxidation by the cubic, layered and spinel forms of lithium cobalt oxides. *Energy Environ. Sci.*, 9(1):184–192, 2016.

[22] M. Huynh, D. K. Bediako, and D. G. Nocera. A functionally stable manganese oxide oxygen evolution catalyst in acid. *J. Am. Chem. Soc.*, 136(16):6002–10, 2014.

[23] T. Takashima, K. Hashimoto, and R. Nakamura. Mechanisms of pH-dependent activity for water oxidation to molecular oxygen by mno_2 electrocatalysts. *J. Am. Chem. Soc.*, 134(3):1519–27, 2012.

[24] Z. P. Nie, D. K. Ma, G. Y. Fang, W. Chen, and S. M. Huang. Concave Bi_2WO_6 nanoplates with oxygen vacancies achieving enhanced electrocatalytic oxygen evolution in near-neutral water. *J. Mater. Chem. A*, 4(7):2438–2444, 2016.

[25] C. Ling, R. Zhang, and H. Jia. Quantum chemical design of doped $Ca_2MnAlO_{(5+\delta)}$ as oxygen storage media. *ACS Appl. Mater. Interfaces*, 7(26):14518–27, 2015.

[26] J. Suntivich, K. J. May, H. A. Gasteiger, J. B. Goodenough, and Y. Shao-Horn. A perovskite oxide optimized for oxygen evolution catalysis from molecular orbital principles. *Science*, 334:1383–1385, 2011.

[27] S. Tang, Y. Liu, and A. Lei. Electrochemical oxidative cross-coupling with hydrogen evolution: a green and sustainable way for bond formation. *Chem*, 4(1):27–45, 2018.

[28] J. Na, B. Seo, J. Kim, C. W. Lee, H. Lee, Y. J. Hwang, B. K. Min, D. K. Lee, H. S. Oh, and U. Lee. General technoeconomic analysis for electrochemical coproduction coupling carbon dioxide reduction with organic oxidation. *Nat. Commun.*, 10(1):5193, 2019.

[29] C. Korzeniewski and C. L. Childers. Formaldehyde yields from methanol electrochemical oxidation on platinum. *J. Phys. Chem. B*, 102:489–492, 1998.

[30] C. L. Childers, H. Huang, and C. Korzeniewski. Formaldehyde yields from methanol electrochemical oxidation on carbon-supported platinum catalysts. *Langmuir*, 15:786–789, 1999.

[31] J. J. Barber. Process for the electrochemical synthesis of ethylene glycol from formaldehyde, 1983.

[32] N. L. Weinberg and D. J. Mazur. Electrochemical hydrodimerization of formaldehyde to ethylene glycol. *J. Appl. Electrochem.*, 21:895–901, 1991.

[33] A. Funakawa, I. Yamanaka, S. Takenaka, and K. Otsuka. Selectivity control of carbonylation of methanol to dimethyl oxalate and dimethyl carbonate over gold anode by electrochemical potential. *J. Am. Chem. Soc.*, 126:5346–5347, 2004.

[34] A. Funakawa, I. Yamanaka, and K. Otsuka. Active control of methanol carbonylation selectivity over Au/carbon anode by electrochemical potential. *J. Phys. Chem. B*, 109:9140–9147, 2005.

[35] I. Yamanaka. Electrocatalytic synthesis of dmc over the Pd/VGCF membrane anode by gas–liquid–solid phase-boundary electrolysis. *J. Catal.*, 221(1):110–118, 2004.

[36] M. C. Figueiredo, V. Trieu, S. Eiden, and M. T. M. Koper. Spectro-electrochemical examination of the formation of dimethyl carbonate from CO and methanol at different electrode materials. *J. Am. Chem. Soc.*, 139(41):14693–14698, 2017.

[37] M. Šarić, B. Jane V. Davies, N. C. Schjødt, S. Dahl, P. G. Moses, M. Escudero-Escribano, M. Arenz, and J. Rossmeisl. Catalyst design criteria and fundamental limitations in the electrochemical synthesis of dimethyl carbonate. *Green Chem.*, 21(22):6200–6209, 2019.